EES Catalysis

ROYAL SOCIETY OF CHEMISTRY

PAPER

View Article Online
View Journal | View Issue

Check for updates

Cite this: *EES Catal.*, 2025, **3**, 128

Unveiling the origins of the activity gap between rotating disk electrodes and membrane electrode assemblies: Pt seed-mediated iridium-doped octahedral platinum nickel catalysts for proton exchange membrane fuel cells†

Lujin Pan,[a] Jiasheng Lu,[a] Olivia Dunseath,[b] Michal Ronovský,[ac] An Guo,[a] Malte Klingenhof,[a] Xingli Wang,[a] Elisabeth Hornberger,[a] Alex Martinez Bonastre,[b] Harriet Burdett,[b] Jonathan Sharman,[b] Fabio Dionigi*[a] and Peter Strasser*[a]

Received 21st August 2024,
Accepted 18th November 2024

DOI: 10.1039/d4ey00172a

rsc.li/eescatalysis

Proton exchange membrane fuel cells (PEMFCs) offer energy solutions of high efficiency and low environmental impact. However, the sluggish kinetics of the oxygen reduction reaction (ORR) at the cathode limit their commercialization. Pt-based electrocatalysts, particularly octahedral (oh)PtNi bimetallic catalysts doped with additional transition metals, stand out as promising candidates for enhancing ORR rates and overall cell performance. A key challenge in the development and validation of active oh PtNi electrocatalysts is the unsuccessful translation of laboratory-scale catalyst test results, typically assessed using the rotating disk electrode (RDE) method, to practical applications in membrane electrode assembly (MEA) for PEMFCs. Here, we consider a new family of Ir-doped octahedral ORR fuel cell catalysts with very high RDE-based Pt mass activities. First, we designed the catalysts and tuned the catalyst layer properties to achieve the new state-of-the-art performance for oh-PtNi catalysts in PEMFCs. Still, a significant decrease in relative performance with respect to Pt/C when transitioning from RDE into an MEA-based cathode environment was observed. Thus, to better understand this performance loss, we investigated the effects of ionomer–catalyst interactions by adjusting the I/C ratio, the effect of temperature by applying RDE under high temperature, and the effects of acidity and high current density by applying and introducing the floating electrode technique (FET) to shaped nanoalloys. A severe detrimental effect was observed for high I/C ratios, with a behaviour contrasting reference commercial catalysts, while the negative effect of high temperatures was enhanced at low I/C. Based on this analysis, our study not only demonstrates a catalyst with enhanced ORR activity and specifically higher electrochemical surface area (ECSA) among oh-PtNi catalysts, but also provides valuable insights into overcoming MEA implementation challenges for these advanced fuel cell catalysts.

Broader context

The transport sector significantly contributes to greenhouse gas (GHG) emissions, often accounting for over a quarter. Fuel cell vehicles (FCVs) powered by low-carbon hydrogen-fueled proton exchange membrane fuel cells (PEMFCs) offer a promising solution due to their high efficiency and low environmental impact. However, commercialization of PEMFCs faces major obstacles, primarily related to stack costs which are dominated by the cost of the platinum catalyst at the cathode. This is why the design of low Pt-loaded cathodes is crucial for commercialization. Despite recent discovery of highly active Pt-based alloy cathode catalysts, there has remained an unaccounted performance gap between laboratory test environments and cell/stack tests. This contribution explores the origins of this performance gap. Our research focuses on octahedrally-shaped PtNi(Ir) ORR nanoparticle catalysts and addresses the impact of selected materials and operation parameters, such as ionomer–catalyst interactions, temperature effects, and high current density conditions, on their performance in liquid electrolyte cells and correlate this to cell tests. We reveal new correlations that can help overcome barriers to unfold the full performance of new alloy catalysts in practical cells.

---

[a] *Department of Chemisty Technical University Berlin, Berlin, Germany. E-mail: pstrasser@tu-berlin.de*
[b] *Johnson Matthey Technology Centre, Blount's Court, Sonning Common, Reading RG4 9NH, UK*
[c] *The European Synchrotron Radiation Facility, 71 avunue des Matrys-CS 40220, 38041 Grenoble cedex 9, France*

† Electronic supplementary information (ESI) available. See DOI: **https://doi.org/10.1039/d4ey00172a**

Introduction

Proton exchange membrane fuel cells (PEMFC) have emerged as promising clean energy devices due to their high efficiency and low environmental impact. The oxygen reduction reaction (ORR) at the cathode is a pivotal process in PEMFCs, where the sluggish kinetics of this reaction limit the commercialization of PEMFCs and necessitate the use of electrocatalysts, in particular, Pt-based catalysts to facilitate the reaction and enhance overall cell performance.

It has been decades that PtNi bimetallic catalysts have gained considerable attention as highly active candidates for ORR owing to their synergistic effects, improved activity, and cost-effectiveness compared to pure Pt.[1–5] While PtNi catalysts are renowned for their exceptional properties, researchers have extended their investigations to include additional transition metals like cobalt (Co), molybdenum (Mo) and rhodium (Rh), *etc.*[6–11] These innovative combinations aim to elevate catalytic activity and stability, providing fresh insights into the potential of doped PtNi-based catalysts. While the incorporation of other stabilizing transition metals, such as Ir, into Pt and PtNi catalysts was reported experimentally and shown with calculation to stabilize the nanoparticle and enhance the ORR activity, a detailed exploration of their catalytic activity and stability in gas diffusion electrode (GDE) environments at higher current densities or even in single membrane electrode assembly (MEA) fuel cell setups is missing to date.[12–18]

An essential aspect of electrocatalyst development lies in successfully translating promising kinetic results obtained at the liquid-cell level, such as in rotating disk electrodes (RDE), to realistic electrode environments involving an MEA adjacent to porous gas diffusion layers.[19–23] The translation from RDE to MEA brings about various challenges due to differences in operating conditions and catalyst–support interactions.[24–27] Understanding and addressing these challenges are crucial for the practical implementation and commercialization of advanced catalysts. For this reason, alternative techniques to RDE have been developed in recent years.[21,23,28–30] For example, the floating electrode technique (FET) permits the observation of performance differences of oh-PtNi alloys and Pt/C under high electrolyte concentration and high current density.

A number of different parameters have a significant impact on the performance and stability of PEMFCs ORR catalysts, such as the interaction of the ionomer with the nanocatalysts and/or the carbon,[31–33] as well as the influence of acidity and ionomer functional groups over degradation.[34,35] In particular, the weight ratio of ionomer to carbon (referred to as the I/C ratio) affects the ionomer distribution on the catalyst surface, directly influencing the catalytic activity and mass transport within the electrode. Many groups have also focused on the influence of cycling voltage limits on the dissolution mechanism of the nanoparticles during accelerated stress tests (ASTs).[36–38] Most of the works are based on pure Pt catalysts. More understanding is still required for the highly active octahedral-shaped PtNi nanoparticles, and research is ongoing.

Here, we address and clarify some of the physico-chemical and electrochemical origins of the previously unaccounted for RDE to MEA fuel cell catalyst performance gap, which has been hampering the development of viable catalysts for realistic fuel cell environments for the past decades. To achieve this, we selected synthetically optimized shape-controlled Pt-based ORR catalysts and correlated their RDE and MEA performance with respect to the ionomer to catalyst ratio (I/C), testing temperature, and the current density. These three important fuel cell parameters were chosen, because they usually vary widely between RDE and MEA tests.

More specifically, we introduce a family of shape-controlled octahedral Ir-doped PtNi nanoparticles and utilize them to conduct a comparative investigation of their catalytic ORR reactivity between 3-electrode liquid-electrolyte setups, such as RDE and FET, and single PEM MEA fuel cell environments. Of particular focus are the challenges associated with the translation of catalyst performance from RDE to MEA setups and potential strategies to overcome them effectively are discussed. The discussion is supported by a thorough examination of the influence of I/C ratios and temperature on the catalytic performance and overall cell efficiency. Insights into the challenges associated with the translation from RDE to MEA are provided through performance and efficiency data obtained from liquid-electrolyte FET experiments at high current density (almost three orders of magnitude larger than RDE). Finally, MEA single fuel cell data are presented and analyzed.

Together, this study provides an improved understanding of factors such as I/C ratio and acidity influencing catalytic ORR activity, explores novel catalyst compositions by combining seed-mediated Pt alloy synthesis methods using Ir dopants, and addresses the still unsolved challenge of translating RDE performance into MEA environments. By doing so, this study contributes significantly to the advancement of PEMFC technology.

Results and discussion

We compare and contrast the synthesis–structure–performance relationships of shape-controlled, octahedral Ir-doped bimetallic PtNi nanoparticles (referred to as "oh-PtNi(Ir)") prepared with and without the assistance of pre-formed pure Pt nano-sized seed particles supported on high surface area carbon support. After a brief discussion of synthesis–structure–reactivity relations of non-seed-mediated PtNi(Ir) electrocatalysts, we will move to the discussion of the results of seed-mediated Pt alloy nanoparticle synthesis and their performance evaluation. Results and conclusions obtained from the non-seed-mediated catalyst studies were the origin of our continued interest in this family of nanostructured Pt alloy materials and led to studies into seed-mediated Pt alloy nanocatalysts described further below.

Non-seed-mediated oh-PtNi(Ir) nanoparticle catalysts

Shape-controlled, octahedral, Vulcan® XC72R carbon supported Ir-doped oh-PtNi(Ir) nanoparticles with Pt weight loadings around 20 wt% were synthesized in one single step using an autoclave-based solvothermal preparation technique detailed in the ESI.†

Table S1 (ESI†) presents compositional data of the carbon-supported oh-PtNi(Ir).[3,8,9] Its X-ray diffraction (XRD) pattern in Fig. S1 (ESI†) suggests a single-phase PtNi(Ir) alloy with the expected fcc crystal structure. The catalyst was evaluated for its electrocatalytic ORR performance in a 3-electrode RDE environment. Results on the catalytic ORR reactivity and stability tests using a RDE setup are shown in Fig. 1a and b. The initial Pt-based mass activity (MA) at 0.9 V_{RHE} is quite high reaching almost 3 A mg_{Pt}^{-1}. After the stability test, the MA presents a drop of ∼44%, while the CO stripping-based electrochemical surface area (ECSA-CO) remained essentially constant (with only a minor increase observed, within error bars).[9] The ECSA-CO of oh-PtNi(Ir) was greater than 50 $m^2\ g_{Pt}^{-1}$, both at the beginning of life (BoL) and after an accelerated voltammetric stress test. This is unexpected considering that the average particle size derived from transmission electron microscopy (TEM) in Fig. 1c was 7.0 ± 1.7 nm, and, as such, larger than other metal-doped PtNi octahedra of our previous study.[7,9,11] Fig. 1c and d display the morphological structure of the carbon-supported oh-PtNi(Ir) from their pristine as-prepared state to their state after the AST. The octahedral nanoparticles largely maintained their morphological octahedral structure. This observation and the negligible change in ECSA suggest that Ni leaching might be the cause for the MA loss.

To better understand how the Ir dopant influenced the ECSA of oh-PtNi(Ir), we utilized X-ray absorption spectroscopy (XAS) to gain insight into the oxidation state of the Ir dopant atoms in the alloy. In Fig. S2 (ESI†), the XAS data provided valuable information regarding the presence and state of Ir in the catalyst. Given the limited abundance of iridium (Ir), achieving a thorough analysis of the XAS data proved challenging, thus impeding the acquisition of more detailed information. However, it is obvious that the Ir L-edge white line and the portion of the spectrum up to ∼100 eV just above the edge was not overlapping with the Ir foil, suggesting that the Ir dopant atoms in our sample were not in metallic form, but, most likely, surrounded by oxygen ligands, like in Ir oxides. Thus, these atoms are not alloyed with the PtNi metallic core of the nanoparticles, and we expect these sites to be at the surface (or near surface). Moreover, to verify a possible contribution of Ir to the ECSA, we synthesized and investigated the electrocatalytic properties of carbon-supported Ir seed particles. As shown in Fig. S3 (ESI†), the catalyst surface area of Ir/C was evaluated by both hydrogen adsorption/desorption region and CO stripping. ECSA-CO values ranged at 57.5 ± 20.4 $m^2\ g_{Ir}^{-1}$. As measured in ICP-OES, the content of Ir in oh-PtNi(Ir) was only around 0.4 wt%. Given the surface doping, we can safely

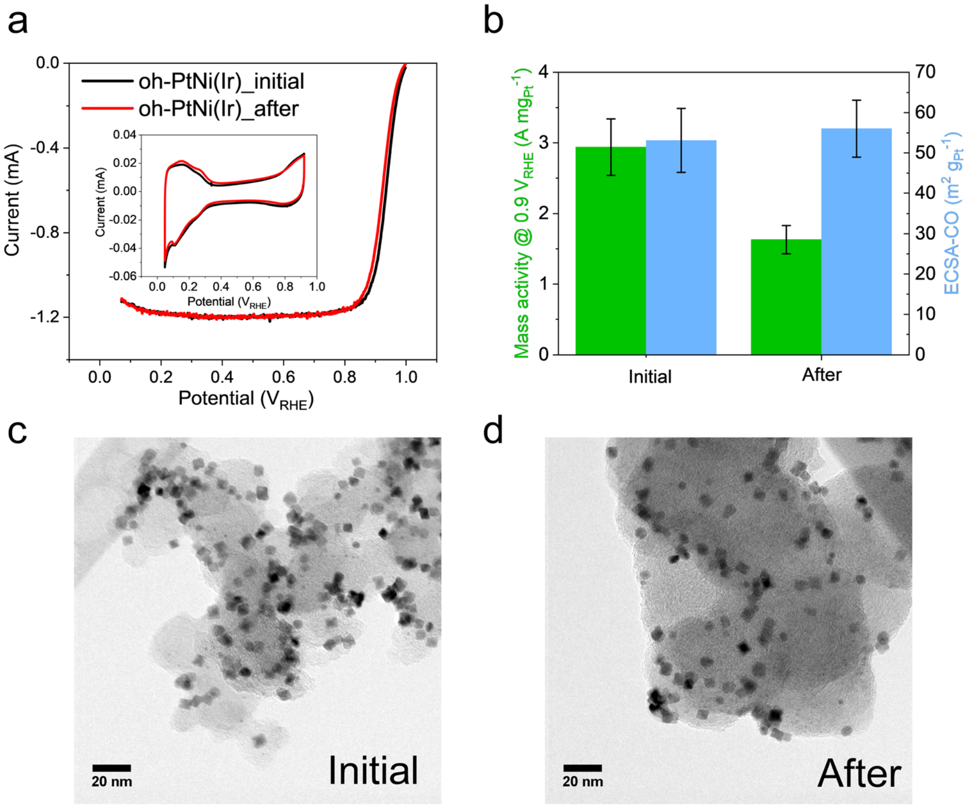

Fig. 1 Electrochemical performance and morphological structure of non-seed oh-PtNi(Ir) supported on Vulcan® XC72R. (a) Linear sweep voltammetry (LSV), scanning rate 20 mV s^{-1}. The black solid line represents the LSV before AST, 10k cycles between 0.6 to 0.925 V_{RHE}, scanning rate 100 mV s^{-1}; the red solid line represents the LSV after AST. In the inset is the cyclic voltammetry, before and after the AST. RDE measured in 0.1 M $HClO_4$. (b) Summary of the mass activity and ECSA-CO before and after AST. (c) and (d) TEM images of non-seed oh-PtNi(Ir) as prepared (c) and after the AST (d).

assume that the Ir surface concentration was higher than that of the bulk. Therefore, the enhancement of ECSA-CO could also originate from the presence of surface Ir dopants *via* an electronic effect or strain effect. Overall, these preliminary studies of oh-PtNi(Ir) nanoparticles revealed significantly enhanced Pt-based catalytic ORR mass activities compared to conventional state-of-the-art binary PtNi alloys, coupled to favorable ECSA values compared to previously reported non surface-doped binary oh-PtNi alloy ORR electrocatalysts.[39]

These non-seed-mediated oh-PtNi(Ir) results, in particular the high ECSA-CO values, prompted and motivated us to continue to investigate Ir-doped PtNi octahedra as promising candidates for cathode catalysts in PEMFC, since ECSA is an important metric for translation to high-performing MEAs. Using seed mediation as a directed particle synthesis technique, we also expected to be able to enhance the Pt weight loading above 20 wt% on the carbon support. Electrocatalysts with insufficient Pt weight loadings result in thick electrode catalyst layers on membranes when deployed in single-cell fuel cells. This, in turn, causes mass transport losses across the catalyst layer associated with voltage losses.

Seed-mediated oh-PtNi(Ir) nanoparticle catalysts

In order to enable higher Pt weight loadings on low and high surface area carbon supports, we prepared carbon-supported shape-controlled octahedral oh-PtNi(Ir) nanoparticles by employing a seed-mediated nanoparticle growth method, the details of which are provided in Fig. S4 (ESI†). We used Carbon Vulcan® XC72R (V) and Ketjen Black EC300 (K) as low and high-surface area carbon supports, respectively. The seed-mediated synthesis technique enabled the preparation of carbon-supported oh-PtNi(Ir) nanoparticles with a Pt weight loading of around 26–30 wt%, considered high for shape-controlled octahedral nanocatalysts. The V-supported and the K-supported seed-mediated oh-PtNi(Ir) nanocatalysts are henceforth referred to as "V30" and "K30", where 30 refers to the nominal 30% Pt loading by weight. The elemental metal composition of all oh-PtNi(Ir) catalysts discussed below was kept similar and followed closely the favorable Pt : Ni : Ir ratio evaluated in preliminary non-seed-mediated study shown in Table S1 (ESI†), in particular a Pt : Ni molar ratio of ~70 : 30 with an Ir dopant level of < 1 at % (see Table S2, ESI†). In Fig. S5 (ESI†), the XRD patterns indicate that the composition and crystal structure of both samples are comparable. The morphology and particle size distribution of the V30 and K30 catalysts on their carbon supports were investigated by TEM, Fig. 2a and b. The TEM images revealed that both V30 and K30 exhibited the expected octahedral shape, with sizes of 5.4 ± 2.3 nm and 4.7 ± 0.9 nm, respectively, with good local distribution. However, an interesting observation was the difference in size distribution between the two samples, with a more significant tail at larger sizes for V30 (insets of Fig. 2a and b). This contrast in size distribution could be attributed to differences in the solid carbon structure or porous structure within these catalysts, since Ketjen Black is known to possess a significant fraction of micropores compared to Vulcan.[40]

To compare distinct synthesis methods and distinct dopant atoms, we contrasted our seed-mediated oh-PtNi(Ir) V30 and K30 with our non-seed-mediated oh-PtNi(Ir) and non-seed-mediated Rh-doped PtNi octahedra, oh-PtNi(Rh), from our previous work.[11] The latter two catalysts showed a particle size of 7.0 ± 1.7 nm and 6.3 ± 1.1 nm, respectively, exceeding those of the two seed-mediated catalysts V30 and K30.[11] This variation in size distribution suggests that the use of seeds may have led to smaller nanoparticles compared to non-seed mediation, even with a larger Pt weight loading.

To investigate the electrocatalyst activity and stability of the two seed-mediated oh-PtNi(Ir) samples V30 and K30, linear scan voltammetry (LSV) was conducted followed by ASTs between 0.6 V_{RHE} and 0.925 V_{RHE} in an N_2-saturated 0.1 M $HClO_4$ solution with a scan rate of 100 mV s^{-1}. In Fig. 2c, we compare the electrochemical performance of V30 and K30 catalysts. Additionally, the inset shows cyclic voltammetry (CV) data before and after AST. The results from these analyses reveal that both samples exhibited favorable and comparable performance.

As summarized in Fig. 2d, V30 generally exhibited a smaller ECSA-CO than K30. Nonetheless, both catalysts exhibited very high ECSA-CO of > 70 $m^2\ g_{Pt}^{-1}$, with K30 showing even > 85 $m^2\ g_{Pt}^{-1}$. Such high ECSAs indicate small particle sizes, possibly due to seed-mediated synthesis and the presence of Ir dopant.

The variation in ECSA-CO values between the two seed-mediated catalysts can be attributed to the varying surface area of the carbon support material. The surface area of the carbon support plays a significant role in confining the particle sizes and their distribution, as seen in the TEM histograms in Fig. 2a and b. For example, as discussed before, the tail in the V30 size distribution at large sizes (~8–14 nm) is conspicuously absent in K30, which features larger surface area and porosity.

The V30 catalyst revealed a slightly higher initial MA than K30, which could be due to the slightly higher Ni : Pt ratio.[41] After AST, the MA of both catalysts still remained around the high values of 1.3 A mg_{Pt}^{-1}. Regarding activity losses, K30 (18.7% of mass activity loss) preserved its performance better than V30 with a ca 30.0% loss.

Finally, in Fig. 2d, V30 and K30 are compared with oh-PtNi(Mo) and a PtNi refernce as well as a commercial Pt/C in a MA *versus* ECSA plot. Both Ir-doped oh-PtNi(Ir) catalyst are located in a region of high MA compared to Pt/C and of much higher ECSA compared to a non-seed-mediated oh-PtNi(Mo).[9] Fig. 2d suggests that K30 and V30 oh-PtNi(Ir) catalysts are very promising catalyst candidates to be deployed in a single MEA, allowing high MA and possibly high current density performance.

MEA single fuel cell performance tests

To evaluate the cell performance of the seed-mediated ORR catalysts in fuel cell cathodes, we conducted MEA tests on both oh-PtNi(Ir) samples together with Pt/C and PtNi/C as reference materials. The polarization curves in H_2/O_2 feeds are shown in Fig. 3a to evaluate the catalyst activity at low current densities. The comparison of the Pt mass activities under H_2/O_2 at 0.9 V cell potential demonstrated that V30 and K30 performed equally well or more active than a commercial state-of-art Pt/C catalyst. The mass activity of Pt/C was 0.27 A mg_{Pt}^{-1}, while the MAs of K30 and V30 were 0.37 A mg_{Pt}^{-1} and at 0.27 A mg_{Pt}^{-1}

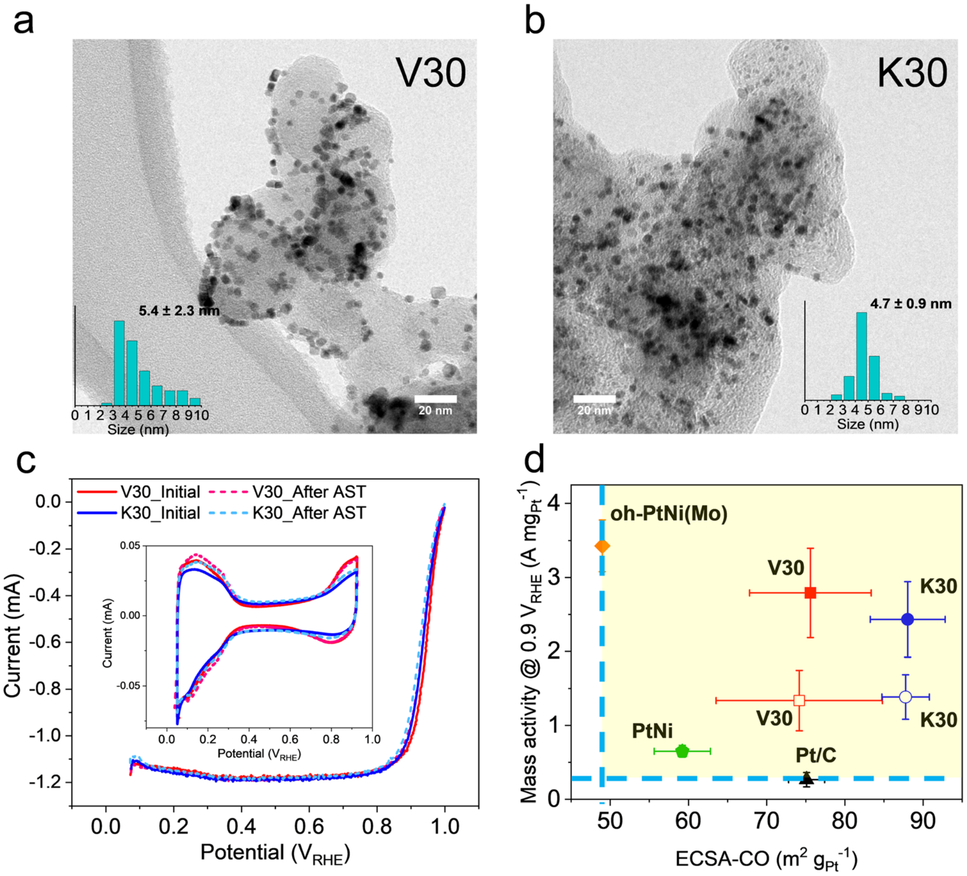

Fig. 2 TEM images of (a) V30 and (b) K30. In the inset is the histogram for nanoparticle size. (c) RDE LSV of V30 and K30, scanning rate 20 mV s^{-1}. The solid lines represent the LSV before the AST, 10k cycles between 0.6 to 0.925 V$_{RHE}$, scanning rate 100 mV s^{-1}; the dashed lines for the LSV after AST. In the inset, the cyclic voltammetry for V30 and K30 is shown, before and after the AST. RDE measured in 0.1 M $HClO_4$. (d) Mass activity measured at 0.9 V$_{RHE}$ of V30 and K30 in RDE as a function of corresponding ECSA-CO before and after AST. Solid symbols are initial electrochemical performance; hollow symbols denote results after AST. V30 sample is marked as a red square; the K30 sample is a blue circle; oh-PtNi(Mo) is a yellow diamond; Pt/C is a black triangle; PtNi reference is a green pentagon. Data for oh-PtNi(Mo) adapted from ref. 9. Solid symbols represent the catalytic performance at the beginning of life (BoL) and after AST, the hollow symbols show the performance at the end of life (EoL).

respectively. The MA of a non-commercial dealloyed PtNi/C was 0.53 A mg$_{Pt}^{-1}$, demonstrating a very active reference catalyst. We note that the experimental MAs of the two oh-PtNi(Ir) catalysts are consistently close to each other, both in RDE and in MEA environments. However, while RDE testing indicated a more than sevenfold increase in activity compared to Pt/C, MEA testing showed a comparable performance. To better conceptualize this performance difference in various test scenarios, we introduce the term enhancement factor. This term helps quantify and describe the increased activity of the oh-PtNi(Ir) samples compared to Pt. While the RDE technique is useful for a qualitative pre-screening of oh-PtNi alloys within the oh-PtNi(Ir) family of catalysts, providing their intrinsic catalytic potential, yet the RDE analysis continues to be unable to predict the single cell MEA performance between different families of catalysts.

In Fig. 3b, the polarization curves in H_2/Air feeds are shown to evaluate the general cell performance. The superior performance of Pt/C could be related to the twofold higher geometric Pt loading of the catalyst. V30 performed less actively at low current density. However, the polarization curve of V30 approached that of K30 at around 300 mA cm$_{geo}^{-2}$. Importantly, V30 outperformed the PtNi/C around 1300 mA cm$_{geo}^{-2}$. Finally, K30 and V30 reached 1500 mA cm$_{geo}^{-2}$ and 1700 mA cm$_{geo}^{-2}$ at 0.6 V, respectively. The V30 MEA exhibited outstanding current density performance, surpassing the values reported in prior studies under similar conditions. These results highlight the exceptional potential of octahedrally-shaped nanoparticles for fuel cell applications. While MEA performance can vary depending on operating factors such as gas flow rates, pressures, and humidity, the performance achieved here demonstrates the significant advancements made in this work. It is important to consider these operational details when comparing results. Nonetheless, the V30 MEA still stands as a noteworthy achievement within the field.

The ECSA values were measured using a cell-based CO stripping method and will be referred to as ECSA-CO$_{MEA}$. The ECSA-CO$_{MEA}$ of V30 was 48.2 m^2 g$_{Pt}^{-1}$ and that of K30 was 65.8 m^2 g$_{Pt}^{-1}$. The high current density performance is made possible by these relatively high ECSA values,[42] which are higher than that reported for oh-PtNiMo (26 m^2 g$_{Pt}^{-1}$) or oh-PtNiRh (30 m^2 g$_{Pt}^{-1}$). The major improvement over previously reported shaped oh-PtNiX fuel cell cathode catalysts extends to

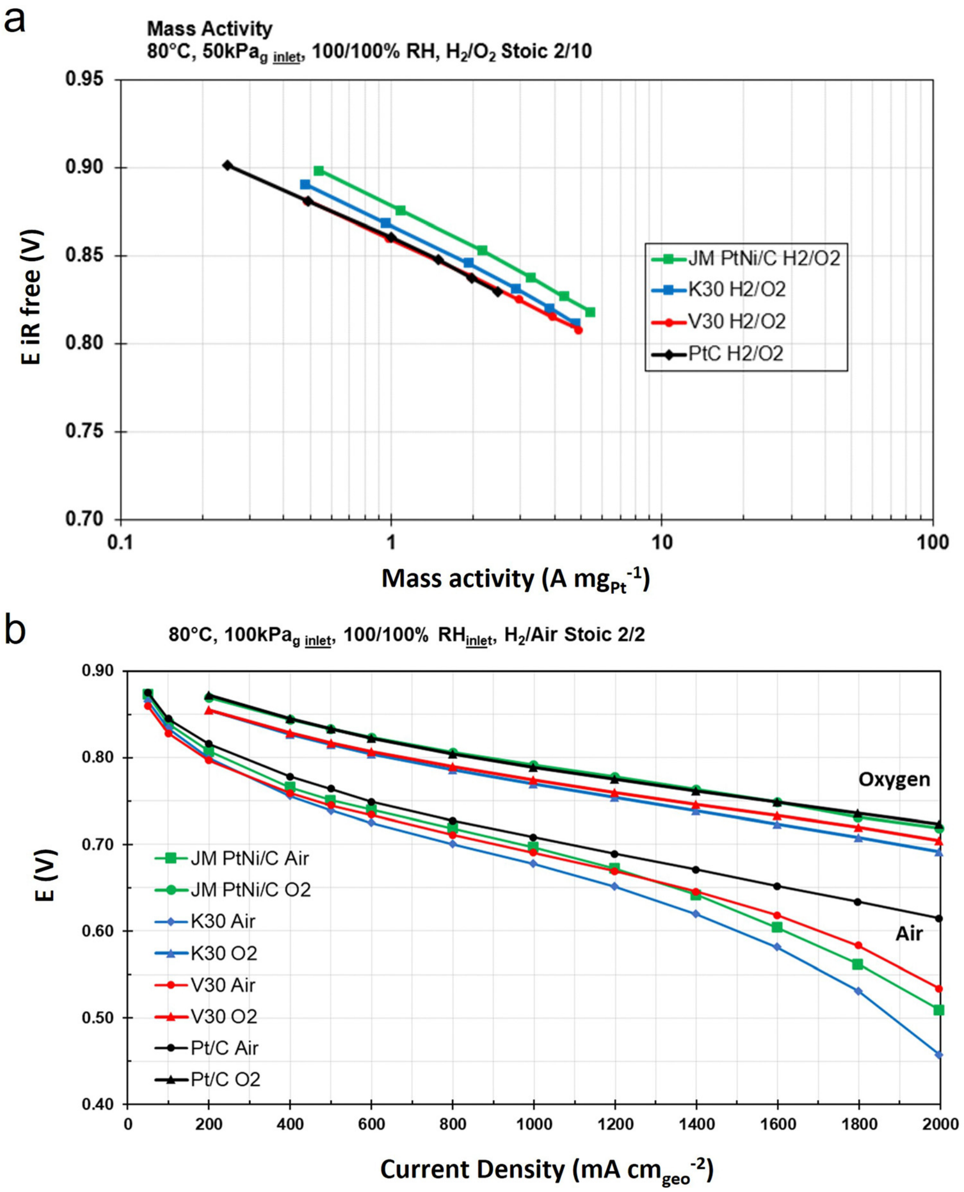

Fig. 3 MEA single-cell performance of K30 (blue), V30 (red), Pt/C (black) and PtNi/C (green) as the cathode and Pt/C as the anode in (a) H_2/O_2 and (b) H_2/air. Polarization curves as a function of current density. The cathode loadings of K30, V30 and PtNi/C were 0.1 mg_{Pt} cm^{-2} and Pt/C was 0.2 mg_{Pt} cm^{-2}. The loading for the anode was 0.1 mg_{Pt} cm^{-2}. 100 RH% cell. Other test details are shown in the figure.

a better nanoparticle distribution and the higher active surface area, which we attribute to the novel seed-mediated synthesis method. While K30 exhibits a higher ECSA compared to V30, its inferior high current density (HCD) performance contradicts conventional expectations. This discrepancy suggests that factors beyond ECSA, such as catalyst particle location on the support material, may significantly influence performance, as well. For instance, K30 was supported on a nanoporous high-surface-area carbon, which may lead to nanoparticle entrapment in small pores, which, in turn, are more susceptible to water flooding under HCD. This leads to a suboptimal access of O_2 and thus reduces HCD performance. As seen in Fig. S6 (ESI†), elemental mapping and TEM images indicate that after MEA test the nanoparticle agglomeration was more severe in V30 than in K30, which also aligned with our assumption about the detailed nanoparticle location in small pores (K30) *versus* the surface of the carbon (V30). Thus, the high performance of V30 may result from particle size benefits of the seed-mediated synthesis method compared to the traditional one-step solvothermal synthesis, coupled to the porous nature of the solid carbon, resulting in less flooding and lower mass transport resistance. The scanning electron microscopy (SEM) images of post-tested MEAs in Fig. S7 (ESI†) showed that the thickness of the catalyst layer of V30 was smaller than that of K30, again something that is related to the carbon structure. Electron probe microanalysis (EPMA) (Fig. S8, ESI†) was also conducted on the post-tested MEAs. Both samples had significant relatively comparable Pt signal on the cathode side, while the dissolution of Ni was observed from the cathode and within the membrane after testing; V30 had a higher signal of Ni dissolution. The elemental mapping after MEA test shown in Fig. S7 (ESI†) also confirms the leaching of Ni, reported previously.[43]

Toward understanding the RDE/MEA performance gaps

Oh-PtNi(Ir) showed the highest ever reported single MEA current density at 0.6 V for an octahedral PtNi fuel cell catalyst. However, the translation between high RDE activity of shaped oh-PtNi alloys into MEA activity has remained challenging. To understand the performance gap from RDE towards MEA, additional tests and analyses were conducted. The concept behind the design of these studies stems from the recognition that the conditions and parameters adopted in the MEA-based cell tests are inherently complex.

The experimental performance gap of oh-PtNi nanoparticle catalysts between RDE and MEA environments can originate from

(1) the high acidity at the triple-phase contact provided by the higher I/C (ionomer-to-catalyst) ratio in MEA,[34,35]

(2) the high operating temperature in MEA tests (*i.e.* 80 °C), compared to room temperature often used in RDE,[26,44]

(3) the ionomer poisoning, which could be more severe in MEA,[32,45]

(4) higher current densities, which might accelerate some of the previously listed effects,[46] or

(5) different upper/lower limit voltage used in operation or during conditioning of the MEA.[38]

Among these, the ionomer poisoning effect is a crucial aspect for shaped nanoparticles, since they can exhibit unique surface structure resulting in outstanding electrochemical activity. When the active alloy particle surface is densely covered by ionomer, the catalytically active facets and surface sites have higher oxygen mass transport resistance, which could be further pronounced by flooding.

Effects of higher I/C ratios

To gain a deeper understanding of how the I/C ratio influences catalyst behavior, we have isolated and examined this specific parameter using well designed RDE experiments. More specifically, we have prepared electrode films by drop casting inks of both V30 and K30 at varying I/C ratios, namely 0.14 (standard ratio for RDE inks), 0.6 and 1.0. These electrode films of the as-prepared samples were compared to two other samples, which were obtained by scraping the catalysts from a PTFE substrate after printing. The printing procedure and ink recipe used were the same as those for preparing MEAs for single-cell tests

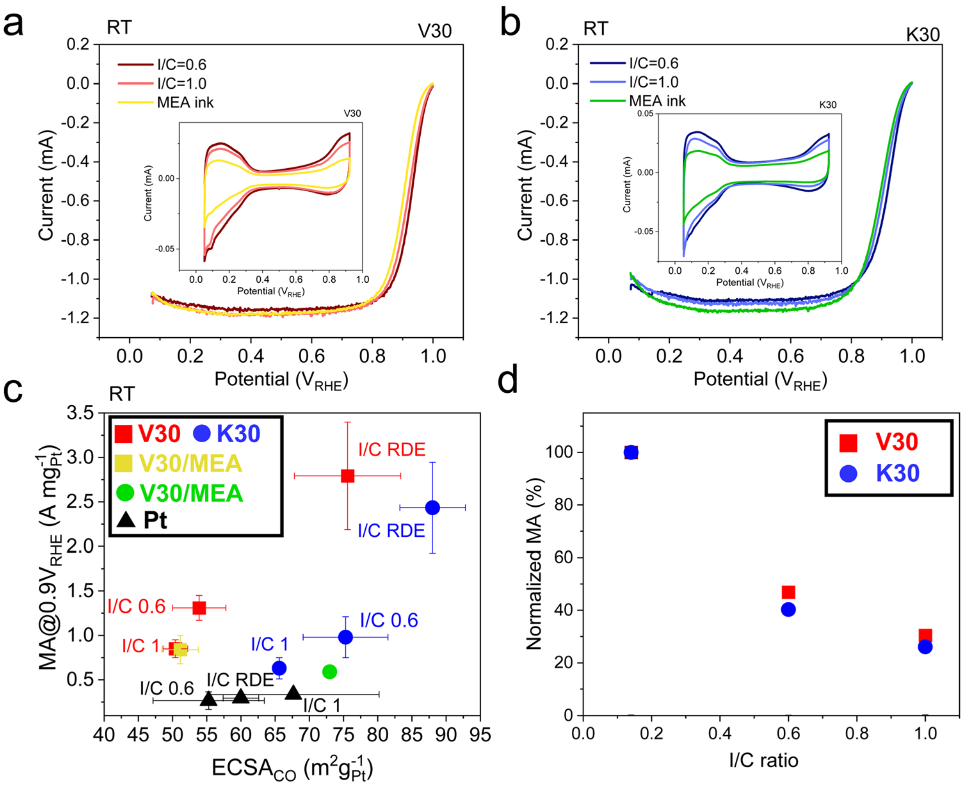

Fig. 4 RDE I/C ratio study under room temperature (RT). LSV of samples with different I/C ratio ink recipe (standard RDE recipe used in this study, 0.6 and 1.0) compared with electrodes fabricated with powders obtained after drying inks prepared with formulation for MEA (MEA ink) and operated under RT for (a) V30 and (b) K30, scanning rate 20 mV s^{-1}. In the insets are the cyclic voltammetry (CV) respectively. RDE recipe corresponds to an I/C ratio of around 0.14. (c) Mass activities measured at 0.9 V$_{RHE}$ plotted *versus* ECSA-CO. Squares stand for V30 samples; red for I/C ratio of RDE, 0.6 and 1; while yellow for MEA-ink treated V30 catalyst powder. Circles for K30 samples; blue for I/C ratio of RDE, 0.6 and 1, while green for MEA-ink treated K30 catalyst powder. Black triangles are data points for Pt reference catalyst. (d) Normalized MA at 0.9 V$_{RHE}$ plotted *versus* I/C ratio of V30 and K30. Red squares for V30; blue circles for K30. Electrolyte used was 0.1 M $HClO_4$.

(Fig. 4a and b and Fig. S9, ESI†). We refer to these samples as "V30/MEA ink" and "K30/MEA ink". The compositional data of V30/MEA ink and K30/MEA ink are included in Table S2 (ESI†). Although the Pt weight percentage decreased due to the addition of ionomer, the compositional ratio did not change much in both samples.

The catalyst MAs of V30, K30, and Pt were evaluated and plotted *versus* ECSA-CO values as shown in Fig. 4c. Strikingly, the trends of the V30 and K30-based catalyst films were very different from that of the Pt/C catalyst film. The Pt/C catalyst films maintained both their MA and, within the experimental error, their ECSA-CO values (see Fig. 4c and Fig. S10, ESI†) with changing I/C ratios, as reported in other studies.[45,47] By contrast, the V30 and K30 catalyst films suffered severe MA losses as the ionomer ratio was increased in the ink. We note that, despite the losses, the MA values of the two oh-PtNi(Ir) catalyst films remained quite high, with V30 at I/C = 1 displaying an enhancement factor of around 2.6× with respect to Pt, while for K30 the factor was close to 2×. Interestingly, V30 and K30 seem to show, within the error, analogous trends in the MA decay as a function of CO-ECSA at different I/C ratios, which additionally shows that also the CO-ECSA is decreasing with increasing I/C ratio. The data measured using the MEA ink also fit well in the same MA and ECSA-CO range, confirming this trend. Moreover, to understand the deactivation mechanism better, Fig. 4d exhibits the relationship between the normalized MAs and the I/C ratios for the two oh-PtNi(Ir) catalysts. For V30 and K30, the MAs reduced to more than half from I/C ratio 0.14 to 0.6, and only ~30% of the mass activity was sustained with the I/C ratio raised to 1. It is evident, that high ionomer surface coverage on the facets, possibly coupled to a leaching effect in the final MEA is one of the bottlenecks for translating the highly active oh-shaped PtNi alloys into MEA high performance.[11]

Effect of higher temperatures

Elevated fuel cell operating temperatures are an important factor in observed activity losses in MEA environments.[48] To better understand the I/C RDE study with respect to the MEA results, we have conducted RDE tests of V30 (Fig. 5a) and Pt reference catalyst (Fig. S12, ESI†) with different I/C ratios at a higher temperature (HT) of 80 °C. Fig. 5a and b report the experimental HT data for both V30 and Pt catalysts and demonstrates that ECSA-CO measurement at 80 °C (Fig. S11 and S12, ESI†) were in general smaller than those obtained at RT. Also, the ECSA-CO values of V30 (Fig. 5c) remained roughly the same within the error at varying I/C ratios. As to catalytic

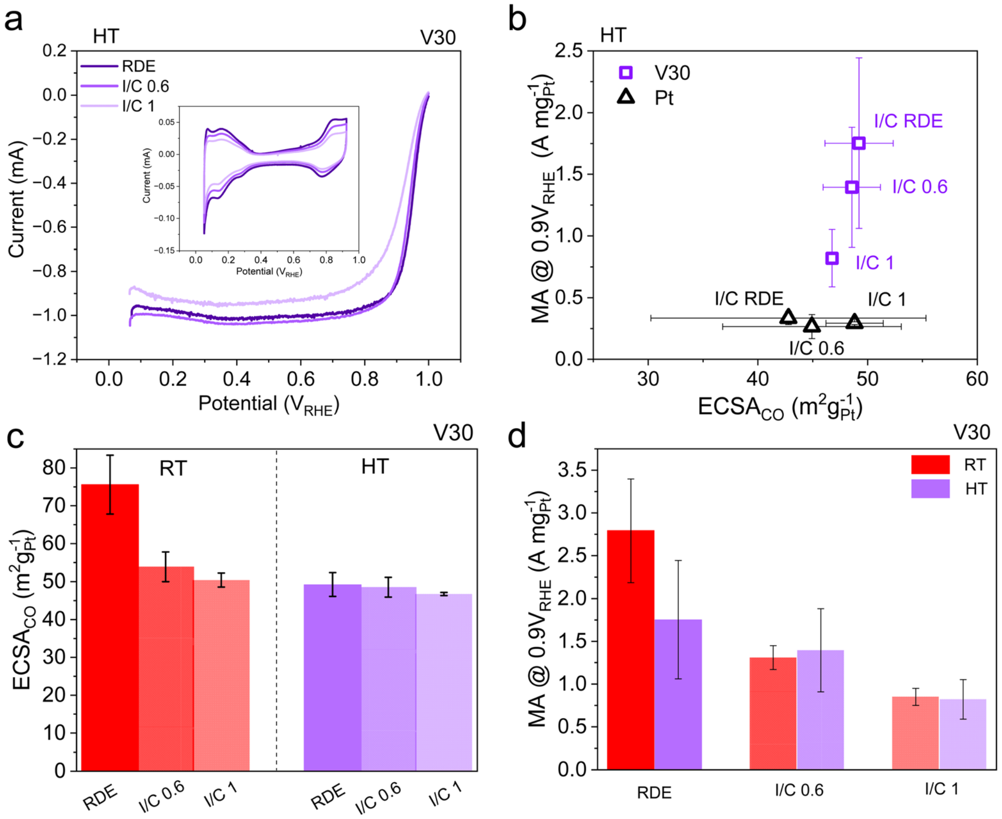

Fig. 5 RDE I/C ratio study under high temperature (HT). LSV of samples with different I/C ratio ink recipe, 0.6 and 1.0 and with MEA treated catalyst powders, operated under RT for (a) V30 and in the insets are the CV, scanning rate 20 mV s^{-1}. RDE electrode ink recipe corresponds to an I/C ratio of around 0.14. (b) Mass activities measured at 0.9 V$_{RHE}$ plotted *versus* ECSA-CO. Purple hollow squares stand for V30 sample; black hollow triangles are data points for Pt reference catalyst. (c) Comparison of ECSA-CO for V30 under RT and HT. (d) Comparison of MA for V30 under RT and HT. Electrolyte used was 0.1 M HClO$_4$. RDE measurements were performed in a jacketed cell, in the outer jacket, 80 °C water was pumping flowing during the test, the temperature difference between electrolyte and heating Mantel was less than 2 °C.

activity, Pt/C at 80 °C was similarly active as at lower temperature (Fig. 5d). This is in contrast to V30, which suffered a decrease in MA at low I/C ratio under HT.

When we compare the ECSA-CO data of V30 at HT and RT (Fig. 5c), we can see the sensitivity of oh-PtNi(Ir) to higher I/C ratio at RT, while ECSA-CO at HT is not influenced by I/C. This relation has not been studied before and provides new insights into temperature-ECSA dependence and thus, helps in understanding the significant differences between RDE and MEA fuel cell measurements. As for surface area, the ECSA-CO values at RT approached those at HT for increasing I/C ratios. This could be due to that more severe catalyst degradation happen under HT, such as metal leaching or catalyst restructure. Regarding activity, the gap between the MAs under RT and HT narrowed, as well, (Fig. 5d), as the I/C ratio increased. This was because the RT MA suffered large losses relative with larger I/C ratio. For instance, V30 at I/C = 1 was merely 2.4× more active than Pt at the same I/C ratio, a fractional enhancement compare to I/C ratios of RDE experiments. So, more generally, we can conclude that the lower the I/C ratio, the larger the gap between HT and RT data. In other words, temperature matters less at high I/C ratios.

The specific activity (SA) data in Fig. S13 (ESI†) showed a similar trend. This observation implies that for active oh-PtNi(Ir) samples, the RT-RDE data at high I/C ratio might be closer to high temperature performance, strongly suggesting the practical value of utilizing higher I/C ratios in RDE studies in the future. These RDE data would more accurately reflect the activity at high temperature of single cell environments. Conversely, translating catalytic ORR activity from RDE conditions into MEA set ups might be better achieved using lower I/C ratios in MEA. Therefore, a strategic balance must be sought, favoring operation using lower temperature and reduced I/C ratios compared to tests of conventional PtNi alloys.

Effect of higher current densities

Another obstacle to successful deployment of highly RDE-active PtNi alloys in equally active MEAs is the high acidic environment, inducing the leaching of transition metals, therefore causing damage to the morphology and metal cation poisoning into the ionomer and membrane. The high current densities in the MEA environment could accelerate further degradation processes. To study this, we adopted the floating electrode technique (FET), which allows electrocatalysts to achieve high current densities in liquid cell with highly concentrated acid electrolyte (>1 M). In contrast to RDE, where the finite solubility of O_2 in the liquid electrolyte gives rise to mass transport limitations, the gas-permeable electrode of FET enables sufficient gas supply resulting in lower mass transport limitation (essentially negligible for the achieved current densities), as well as low proton resistance due to high electrolyte concentration.[21,28,29] In Fig. 6a, it is clear that unlike RDE, no diffusion limited current due to mass transport limitation is observed. We note that our oh-PtNi(Ir) catalyst was able to achieve current densities above 1 A cm^{-2}_{geo}. Moreover, in Fig. 6b, the mass activity obtained by FET of our oh-PtNi(Ir) is compared with the reference PtNi alloy/C catalyst and the Pt/C. The PtNi catalyst displayed mass activity that is double the one of Pt/C, which is similar to previous RDE reports. In contrast, the oh-PtNi(Ir) was 5× more active than Pt/C, while in RDE oh-PtNi(Ir) showed activity enhancement of a factor of 7×. This demonstrates that in FET as well as in RDE, oh-PtNi(Ir) catalysts showed significant activity advantage over pure Pt catalyst and PtNi alloys and validates their potential benefits in single cells.

Furthermore, the 5× activity enhancement factor *vs.* Pt/C in FET is in contrast with our MEA test results, where oh-PtNi(Ir) catalysts exhibited similar Pt mass activities as pure Pt. Thus, our FET measurements demonstrate that high acidity and high current densities alone do not account for, nor explain, the performance decrease in MEA environment. Notably, the I/C ratio of the inks of the FET measurements was ∼1.1. The absence of a large activity decrease at such high I/C ratio seems at first surprising considering the results of Fig. 5. However, a direct comparison with the I/C RDE study might not be justified here, due to the distinct way of depositing the catalyst in FET *vs.* RDE that results in much lower I/C ratios on the working electrode than in the ink in FET. While high temperature operation and more pronounced ionomer poisoning at higher I/C ratios have a significant impact on the MEA performance of

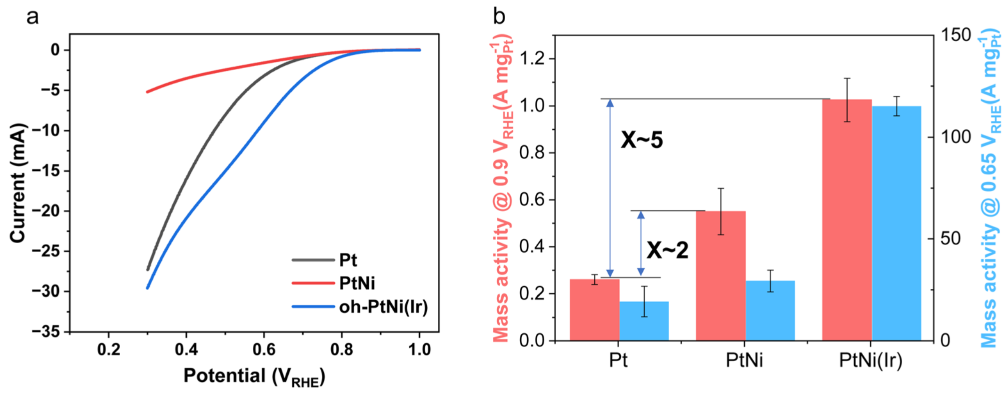

Fig. 6 FET data of Pt/C, PtNi and PtNi(Ir). (a) Comparison of specific ORR polarization curves for Pt/C, PtNi/C and oh-PtNi(Ir) catalysts. (b) Comparison of MAs at 0.9 V_{RHE} and 0.65 V_{RHE}. Pt loading of Pt/C, PtNi/C and oh-PtNi(Ir) catalyst is 4.8, 1.0 and 1.1 μg_{Pt} cm^{-2}, respectively, electrolyte 1.6 M $HClO_4$, sweeping rate 10 mV s^{-1}. The I/C ratio of the inks of the FET measurements was ∼1.1. Measurements were conducted at room temperature.

the oh-PtNi(Ir) catalysts, we suspect that there are more to date elusive reasons, likely related to the electrode fabrication. Studies on catalyst coated membranes (CCM) using PtNi(Ir) nanoparticles have found a drastic compositional decrease in Ni,[38] while in the present study, the ICP-OES (Table S2, ESI†) data exhibited nearly constant nickel content after making and drying the MEA ink. The difference between these FET and MEA results can possibly be ascribed to the elevated temperatures during CCM fabrication *via* hot pressing.

Conclusion

This study has addressed the physico-chemical and electrochemical origins of the insufficiently understood RDE-MEA fuel cell cathode catalyst performance gap, which has been hampering the development of viable catalysts for realistic fuel cell environments for the past decades. More specifically, we have presented experimental results that correlated the RDE and MEA performance of a family of shape-controlled octahedral PtNi(Ir) catalysts, oh-PtNi(Ir). These catalysts were chosen based on their extraordinarily high catalytic activity in RDE environments. Our RDE-MEA correlations focused on the ionomer to catalyst ratio (I/C), temperature, and current density-parameters as variables which usually vary widely between RDE and MEA tests. We expect that this work and the general findings about the origins of the gap between RDE and MEA performance are valid for many other octahedral PtNi systems. This is due to the fact that they mostly suffer from the same main issue, which stems from the challenging retention of Ni atoms.

The present study featured two 30 Pt wt% Ir-doped oh-PtNi(Ir) alloys supported on Ketjen Black KB300 and Carbon Vulcan® XC72R using a novel particle seed-mediated preparation technique. This method offered improved particle size distribution, surface enriched Ir atoms, and higher Pt weight loading which contributed to higher beneficial ECSA values. While a significant enhancement thanks to the surface Ir atoms on the stability of the oh-PtNi(Ir) was not observed, and the effect on the ORR activity was comparable to Rh doping, the higher ECSA of seed-mediated synthesis method turned out to be beneficial to their single PEM fuel cell performance under high current density.

Our samples measured in MEA showed very high current density performance for this family of shaped nanoparticle catalysts. Interestingly, under H_2/air, the V30 catalyst showed the lowest activity at small current densities, but matched the performance of K30 at 300 mA cm_{geo}^{-2} and outperformed PtNi at 1300 mA cm_{geo}^{-2}. Notably, V30 reached 1700 mA cm_{geo}^{-2} at 0.6 V. This may be contributed both by the seed-mediated synthesis and Ir dopant effect.

To investigate the mechanism behind the loss in activity enhancement factor and shed light on the gap between RDE and MEA performance of octahedral shaped nanoparticles, we have conducted a I/C ratio study as well as a FET study and a temperature study. The I/C ratio study showed that different types of catalysts unveil different behaviors with increasing I/C ratios. Unlike Pt-only catalyst, Ir doped octahedral PtNi nanoparticles lost not only surface-active area, but also mass activity with more ionomer content in the inks. This could be because of an ionomer poisoning effect on the catalyst active surface and calls for future atomic-level element specific investigations at the catalyst surface. The MA loss was estimated at $\sim$70% with an increase of I/C from 0.14 to 1. Increasing temperature to 80 °C also caused a decrease in activity, but mainly only at low I/C ratio, while at high I/C ratio close to 1 the percentage loss was similar to the one at RT at parity of I/C. Furthermore, our FET data in concentrated electrolyte revealed that oh-PtNi(Ir) still exhibited 5-folds of activity improvement than Pt. This is interesting, since our MEA single cell tests reveal an enhancement not larger than 2.

Our research reveals that in RDE measurements, the performance of octahedral-shaped PtNi nanoalloys is significantly affected by ionomer content and elevated temperatures, especially at low I/C ratios. Notably, at higher temperatures in RDE, both ECSA and activity levels align more closely with room temperature data at higher I/C ratios ($\geq$0.6), and are more representative of MEA performance. Therefore, for more accurate preliminary RDE screening of the true potential of shape-control nanocatalysts, it is suggested to adopt either high temperature or medium/high ionomer content. Complementarily, optimizing MEA performance might involve using lower I/C ratios and temperatures. Additionally, for shaped PtNi alloy catalysts, the use of very high temperatures in MEA fabrication during hot pressing might cause significant challenges in terms of both composition and morphology, as our RDE temperature study suggests. In general, little research has been conducted on this topic.[49] Therefore, future research should focus not only on optimizing catalyst stability, I/C layer composition and operating conditions, but also on electrode fabrication procedure.

These approaches could benefit the community by providing more reliable pre-screening methodologies and enhancing the overall effectiveness of these catalysts in practical applications.

Data availability

The synthesis and characterization data, including XRD, ICP-OES, UPS, TEM, SEM, EPMA, RDE, FET and MEA measurements, have been included in this article or as part of the ESI.†

Conflicts of interest

There are no conflicts to declare.

Acknowledgements

We thank the GAIA EU project for financial support. The collaborative GAIA EU research and development project has received funding from the Fuel Cells and Hydrogen 2 Joint Undertaking under grant agreement No. 826097. This Joint Undertaking receives support from the European Union's

Horizon 2020 – Research and Innovation Framework Programme, Hydrogen Europe and Hydrogen Europe Research. We also thank the EU project "HIGHLANDER". The HIGHLANDER project is supported by the Clean Hydrogen Partnership and its members Hydrogen Europe and Hydrogen Europe Research under grant agreement No. 101101346. The authors are grateful for the financial support by the Deutsche Forschungsgemeinschaft (DFG) under the grant number HE 7192/1-2. We acknowledge the support of Hitachi High-Technologies. We thank the Zentraleinrichtung Elektronenmikroskopie (ZELMI) of Technische Universität Berlin for their support with TEM measurements. We thank Johnson Matthey Hydrogen Technologies Ltd. (UK) for supporting with the commercial catalyst.

References

1 V. R. Stamenkovic, B. Fowler, B. S. Mun, G. Wang, P. N. Ross, C. A. Lucas and N. M. Markovic, *Science*, 2007, **315**, 493–497, DOI: 10.1126/science.1135941.

2 S. I. Choi, S. Xie, M. Shao, J. H. Odell, N. Lu, H. C. Peng, L. Protsailo, S. Guerrero, J. Park, X. Xia, J. Wang, M. J. Kim and Y. Xia, *Nano Lett.*, 2013, **13**, 3420–3425, DOI: 10.1021/nl401881z.

3 X. Huang, E. Zhu, Y. Chen, Y. Li, C. Y. Chiu, Y. Xu, Z. Lin, X. Duan and Y. Huang, *Adv. Mater.*, 2013, **25**, 2974–2979, DOI: 10.1002/adma.201205315.

4 L. Gan, C. Cui, M. Heggen, F. Dionigi, S. Rudi and P. Strasser, *Science*, 2014, **346**, 1502–1506.

5 X. Huang, Z. Zhao, L. Cao, Y. Chen, E. Zhu, Z. Lin, M. Li, A. Yan, A. Zettl, Y. M. Wang, X. Duan, T. Mueller and Y. Huang, *Science*, 2015, **348**, 1230–1234, DOI: 10.1126/science.aaa8765.

6 R. M. Aran-Ais, F. Dionigi, T. Merzdorf, M. Gocyla, M. Heggen, R. E. Dunin-Borkowski, M. Gliech, J. Solla-Gullon, E. Herrero, J. M. Feliu and P. Strasser, *Nano Lett.*, 2015, **15**, 7473–7480, DOI: 10.1021/acs.nanolett.5b03057.

7 V. Beermann, M. Gocyla, E. Willinger, S. Rudi, M. Heggen, R. E. Dunin-Borkowski, M. G. Willinger and P. Strasser, *Nano Lett.*, 2016, **16**, 1719–1725, DOI: 10.1021/acs.nanolett.5b04636.

8 Q. Jia, Z. Zhao, L. Cao, J. Li, S. Ghoshal, V. Davies, E. Stavitski, K. Attenkofer, Z. Liu, M. Li, X. Duan, S. Mukerjee, T. Mueller and Y. Huang, *Nano Lett.*, 2018, **18**, 798–804, DOI: 10.1021/acs.nanolett.7b04007.

9 F. Dionigi, C. C. Weber, M. Primbs, M. Gocyla, A. M. Bonastre, C. Spori, H. Schmies, E. Hornberger, S. Kuhl, J. Drnec, M. Heggen, J. Sharman, R. E. Dunin-Borkowski and P. Strasser, *Nano Lett.*, 2019, **19**, 6876–6885, DOI: 10.1021/acs.nanolett.9b02116.

10 J. Lim, H. Shin, M. Kim, H. Lee, K. S. Lee, Y. Kwon, D. Song, S. Oh, H. Kim and E. Cho, *Nano Lett.*, 2018, **18**, 2450–2458, DOI: 10.1021/acs.nanolett.8b00028.

11 L. Pan, A. Parnière, O. Dunseath, D. Fongalland, G. Nicolau, C. C. Weber, J. Lu, M. Klingenhof, A. Arinchtein, H.-S. Oh, P.-Y. Blanchard, S. Cavaliere, M. Heggen, R. E. Dunin-Borkowski, A. M. Bonastre, F. Dionigi, J. Sharman, D. Jones and P. Strasser, *ACS Catal.*, 2023, 10–20, DOI: 10.1021/acscatal.3c02619.

12 J. Greeley and J. K. Nørskov, *J. Phys. Chem. C*, 2009, **113**, 4932–4939, DOI: 10.1021/jp808945y.

13 K. Kusunoki, D. Kudo, K. Hayashi, Y. Chida, N. Todoroki and T. Wadayama, *ACS Catal.*, 2021, **11**, 1554–1562, DOI: 10.1021/acscatal.0c04054.

14 K. A. Kuttiyiel, Y. Choi, K. Sasaki, D. Su, S.-M. Hwang, S.-D. Yim, T.-H. Yang, G.-G. Park and R. R. Adzic, *Nano Energy*, 2016, **29**, 261–267, DOI: 10.1016/j.nanoen.2016.05.024.

15 A. L. Strickler, A. Jackson and T. F. Jaramillo, *ACS Energy Lett.*, 2016, **2**, 244–249, DOI: 10.1021/acsenergylett.6b00585.

16 N. Todoroki, H. Watanabe, T. Kondo, S. Kaneko and T. Wadayama, *Electrochim. Acta*, 2016, **222**, 1616–1621, DOI: 10.1016/j.electacta.2016.11.149.

17 T. Yang, G. Cao, Q. Huang, Y. Ma, S. Wan, H. Zhao, N. Li, F. Yin, X. Sun, D. Zhang and M. Wang, *J. Power Sources*, 2015, **291**, 201–208, DOI: 10.1016/j.jpowsour.2015.05.032.

18 K. J. Sawant, Z. Zeng and J. P. Greeley, *Angew. Chem., Int. Ed.*, 2024, **63**, e202312747, DOI: 10.1002/anie.202312747.

19 H. A. Gasteiger, S. S. Kocha, B. Sompalli and F. T. Wagner, *Appl. Catal., B*, 2005, **56**, 9–35, DOI: 10.1016/j.apcatb.2004.06.021.

20 B. Li, J. Wang, X. Gao, C. Qin, D. Yang, H. Lv, Q. Xiao and C. Zhang, *Nano Res.*, 2018, **12**, 281–287, DOI: 10.1007/s12274-018-2211-9.

21 S. Martens, L. Asen, G. Ercolano, F. Dionigi, C. Zalitis, A. Hawkins, A. Martinez Bonastre, L. Seidl, A. C. Knoll, J. Sharman, P. Strasser, D. Jones and O. Schneider, *J. Power Sources*, 2018, **392**, 274–284, DOI: 10.1016/j.jpowsour.2018.04.084.

22 L. Pan, S. Ott, F. Dionigi and P. Strasser, *Curr. Opin. Electrochem.*, 2019, **18**, 61–71, DOI: 10.1016/j.coelec.2019.10.011.

23 T. Imhof, R. K. F. Della Bella, B. M. Stuhmeier, H. A. Gasteiger and M. Ledendecker, *Phys. Chem. Chem. Phys.*, 2023, **25**, 20533–20545, DOI: 10.1039/d3cp02847j.

24 S. Ott, A. Orfanidi, H. Schmies, B. Anke, H. N. Nong, J. Hubner, U. Gernert, M. Gliech, M. Lerch and P. Strasser, *Nat. Mater.*, 2020, **19**, 77–85, DOI: 10.1038/s41563-019-0487-0.

25 V. Yarlagadda, M. K. Carpenter, T. E. Moylan, R. S. Kukreja, R. Koestner, W. Gu, L. Thompson and A. Kongkanand, *ACS Energy Lett.*, 2018, **3**, 618–621, DOI: 10.1021/acsenergylett.8b00186.

26 T. Lochner, R. M. Kluge, J. Fichtner, H. A. El-Sayed, B. Garlyyev and A. S. Bandarenka, *ChemElectroChem*, 2020, **7**, 3545–3568, DOI: 10.1002/celc.202000588.

27 N. Ramaswamy, S. Kumaraguru, R. S. Kukreja, D. Groom, K. Jarvis and P. Ferreira, *J. Electrochem. Soc.*, 2021, **168**, 124512, DOI: 10.1149/1945-7111/ac4374.

28 C. M. Zalitis, D. Kramer and A. R. Kucernak, *Phys. Chem. Chem. Phys.*, 2013, **15**, 4329–4340, DOI: 10.1039/c3cp44431g.

29 X. Lin, C. M. Zalitis, J. Sharman and A. Kucernak, *ACS Appl. Mater. Interfaces*, 2020, **12**, 47467–47481, DOI: 10.1021/acsami.0c12718.

30 K. Ehelebe, N. Schmitt, G. Sievers, A. W. Jensen, A. Hrnjić, P. Collantes Jiménez, P. Kaiser, M. Geuß, Y.-P. Ku, P. Jovanovič,

K. J. J. Mayrhofer, B. Etzold, N. Hodnik, M. Escudero-Escribano, M. Arenz and S. Cherevko, *ACS Energy Lett.*, 2022, **7**, 816–826, DOI: 10.1021/acsenergylett.1c02659.

31 Z. Wen, S. Li, S. Yi, Q. Zhao, Z. Zhu and M. Pan, *Int. J. Electrochem. Sci.*, 2023, **18**(6), 10052, DOI: 10.1016/j.ijoes.2023.100152.

32 H. Ishikawa, Y. Sugawara, G. Inoue and M. Kawase, *J. Power Sources*, 2018, **374**, 196–204, DOI: 10.1016/j.jpowsour.2017.11.026.

33 Y. Qi, Y. Morimoto, M. S. Shibata, Z. Gao, D. C. Sabarirajan, A. T. Haug and I. V. Zenyuk, *J. Electrochem. Soc.*, 2022, **169**, 064512, DOI: 10.1149/1945-7111/ac774f.

34 G. A. Kamat, J. A. Zamora Zeledon, G. Gunasooriya, S. M. Dull, J. T. Perryman, J. K. Norskov, M. B. Stevens and T. F. Jaramillo, *Commun. Chem.*, 2022, **5**, 20, DOI: 10.1038/s42004-022-00635-1.

35 V. Briega-Martos, E. Herrero and J. M. Feliu, *Electrochim. Acta*, 2017, **241**, 497–509, DOI: 10.1016/j.electacta.2017.04.162.

36 S. Cherevko, G. P. Keeley, S. Geiger, A. R. Zeradjanin, N. Hodnik, N. Kulyk and K. J. J. Mayrhofer, *ChemElectroChem*, 2015, **2**, 1471–1478, DOI: 10.1002/celc.201500098.

37 D. J. Myers, X. Wang, M. C. Smith and K. L. More, *J. Electrochem. Soc.*, 2018, **165**, F3178–F3190, DOI: 10.1149/2.0211806jes.

38 M. Ronovsky, L. Pan, M. Klingenhof, I. Martens, L. Fusek, P. Kus, R. Chattot, M. Mirolo, F. Dionigi, H. Burdett, J. Sharman, P. Strasser, A. M. Bonastre and J. Drnec, *ACS Appl. Energy Mater.*, 2023, **6**, 8660–8665, DOI: 10.1021/acsaem.3c01243.

39 C. Cui, L. Gan, M. Heggen, S. Rudi and P. Strasser, *Nat. Mater.*, 2013, **12**, 765–771, DOI: 10.1038/nmat3668.

40 E. N. Gribov, A. N. Kuznetsov, I. N. Voropaev, V. A. Golovin, P. A. Simonov, A. V. Romanenko and A. G. Okunev, *Electrocatalysis*, 2015, **7**, 159–173, DOI: 10.1007/s12678-015-0294-6.

41 M. Xie, M. Shen, R. Chen and Y. Xia, *ACS Appl. Mater. Interfaces*, 2023, **15**, 49146–49153, DOI: 10.1021/acsami.3c10514.

42 A. Kongkanand and M. F. Mathias, *J. Phys. Chem. Lett.*, 2016, **7**, 1127–1137, DOI: 10.1021/acs.jpclett.6b00216.

43 M. Ronovský, M. Myllymäki, Y. Watier, P. Glatzel, P. Strasser, A. M. Bonastre and J. Drnec, *J. Power Sources*, 2024, **592**(1), 233906, DOI: 10.1016/j.jpowsour.2023.233906.

44 T. A. M. Suter, K. Smith, J. Hack, L. Rasha, Z. Rana, G. M. A. Angel, P. R. Shearing, T. S. Miller and D. J. L. Brett, *Adv. Energy Mater.*, 2021, **11**(37), 2101025, DOI: 10.1002/aenm.202101025.

45 K. Shinozaki, Y. Morimoto, B. S. Pivovar and S. S. Kocha, *J. Power Sources*, 2016, **325**, 745–751, DOI: 10.1016/j.jpowsour.2016.06.062.

46 J. Wang, J. Geng, M. Wang, X. Hu, Z. Shao and H. Zhang, *J. Power Sources*, 2022, **521**(15), 230878, DOI: 10.1016/j.jpowsour.2021.230878.

47 K. Shinozaki, J. W. Zack, S. Pylypenko, B. S. Pivovar and S. S. Kocha, *J. Electrochem. Soc.*, 2015, **162**, F1384–F1396, DOI: 10.1149/2.0551512jes.

48 H. Lee, S. Jeong, J. Song, M. Kim, C. Chu, Y. Lee, D. Kim and M. Kim, *J. Mech. Sci. Technol.*, 2023, **37**, 2095–2108, DOI: 10.1007/s12206-023-0345-5.

49 M. Ronovský, O. Dunseath, T. Hrbek, P. Kúš, M. Gatalo, S. Polani, J. Kubát, D. Götz, H. Nedumkulam, A. Satori, E. Petrucco, F. R. Zepeda, N. Hodnik, P. Strasser, A. M. Bonastre and J. Drnec, *ChemRxiv.*, 2024, preprint, DOI: 10.26434/chemrxiv-2024-g9lx2-v2.